PAPER

In situ self-assembly of Ni$_3$S$_2$/MnS/CuS/reduced graphene composite on nickel foam for high power supercapacitors†

Wenbo Li,[ab] Weiming Song,*[a] Haihua Wang [ID] *[b] and Yong-Mook Kang[c]

Transition metal sulfides (TMS), as promising electroactive materials for asymmetric supercapacitors, have been limited due to their relatively poor conductivity and cycle stability. Here ternary Ni$_3$S$_2$/MnS/CuS composites were assembled *in situ* on nickel foam (NF) using a hydrothermal method *via* electrostatic adsorption of Ni$^+$, Mn^{2+} and Cu^{2+} ions on a reduced graphene (rGO) nanosheet template. The chemical structure was characterized by various analytic methods. Ni$_3$S$_2$/MnS/CuS has spherical morphology assembled from closely packed nanosheets, while Ni$_3$S$_2$/MnS/CuS@rGO has a three-dimensional porous spherical structure with much lower diameter because rGO nanosheets can play the role of a template to induce the growth of Ni$_3$S$_2$/MnS/CuS. At a current density of 1 A g^{-1}, the specific capacitance was obtained to be 1028 F g^{-1} for Ni$_3$S$_2$/MnS/CuS, 628.6 F g^{-1} for Ni$_3$S$_2$/MnS@rGO, and 2042 F g^{-1} for Ni$_3$S$_2$/MnS/CuS@rGO, respectively. Charge transfer resistance (R_{ct}) of Ni$_3$S$_2$/MnS/CuS@rGO (0.001 Ω) was much lower than that of Ni$_3$S$_2$/MnS@rGO by 0.02 Ω, and lower than that of Ni$_3$S$_2$/MnS/CuS by 0.017 Ω. After 5000 cycles, the Ni$_3$S$_2$–MnS–CuS@RGO electrode maintains 78.3% of the initial capacity at 20 A g^{-1}. An asymmetric supercapacitor was subsequently assembled using Ni$_3$S$_2$/MnS/CuS@rGO as the positive electrode and rGO as the negative electrode. The specific capacitance of asymmetric batteries was maintained at 90.8% of the initial state after 5000 GCD.

Introduction

The demand for high-performance energy storage devices has attracted intensive attention around the world.[1,2] Among different energy storage devices, supercapacitors are considered to have superior performance due to their superior performance characteristics, including high power density, ultra-fast charge–discharge rate, low maintenance, long service life, excellent stability and safety.[3–5] Based on the interface storage mechanism between the electrode and the electrolyte, the supercapacitors are classified into electric double layer capacitors and pseudocapacitors.[6] The capacity of double layer capacitors and pseudocapacitors mainly depends on the characteristics of the electrolyte, the surface morphology, surface area and structure of the electrodes. Among them, double layer capacitors rely on charge storage for ion adsorption and desorption, while pseudocapacitors rely on charge storage and involve fast

Faraday redox reactions at the electrode/electrolyte interface. Compared with double layer capacitors, pseudocapacitors usually display higher energy density and specific capacitance, transition metal oxides (TMO) and transition metal sulfides (TMS) are generally utilized in pseudocapacitors.[7] It has been reported that the composites of graphene with Ni-, Mn- and Co-rich TMO or TMS show excellent electrochemical performance.[8,9] More importantly, due to multiple oxidation, the ternary transition metal sulfide exhibits greater redox activity and higher specific capacitance than the single transition metal sulfide counterpart.[10–13] However, the application of TMO or TMS is limited due to their relatively poor conductivity and cycle stability.[14,15] The transfer impedance (R_{ct}) of Ni$_3$S$_2$, Ni$_3$S$_2$/MWCNT-NC,[16] Ni$_3$S$_2$/rGO,[17] pure MnS, γ-MnS/rGO-60, a-MnS and a-MnS/N-rGO,[18] Ni$_3$S$_2$/MnS,[19] CuS and CuS-rGO[20] have been reported to be 8.99 Ω, 0.7 Ω, 1.4 Ω, 0.3 Ω, 0.2 Ω, 8.68 Ω, 3.74 Ω, 0.52 Ω, 12.2 Ω and 4.2 Ω, respectively. The solution impedance (R_s) of pure MnS, γ-MnS/rGO-60, Ni$_3$S$_2$/MnS and CuS-rGO are 8.8 Ω, 1.3 Ω, 1.1 Ω, 0.25 Ω and 0.5 Ω, respectively.

In this study, ternary TMS/rGO composites were *in situ* assembled on nickel foam (NF) using hydrothermal method. Ternary TMS/rGO composites were fabricated *via* electrostatic adsorption of Ni$^+$, Mn^{2+} and Cu^{2+} ions on rGO nanosheet, followed by the sulfurization which utilizes thiourea as sulfur source.[21] The objective of this research is to reduce R_{ct} through the incorporation of Cu^{2+} into the binary TMS system and

[a]College of Chemistry and Chemical Engineering, Qiqihar University, Heilongjiang 161006, P. R. China. E-mail: qdsongweiming@163.com

[b]Shannxi Key Laboratory of Chemical Additives for Industry, Shaanxi University of Science and Technology, Xi'an 710021, P. R. China. E-mail: whh@sust.edu.cn

[c]Department of Materials Science and Engineering, Korea University, Seoul 02841, Republic of Korea

† Electronic supplementary information (ESI) available. See DOI: 10.1039/c9ra05435a

utilization of rGO nanosheets as template. On the one hand, CuS and rGO nanosheets can functionalize as template to induce the growth of Ni₃S₂/MnS,[22] forming a three-dimensional porous spherical structure self-assembled by nanosheets, generating a more efficient electron transport structure. On the other hand, CuS electrode exhibits higher conversion efficiency and faster charge transfer. The presence of Cu vacancies in CuS is able to improve the ionic and electronic conduction, as well as the free holes in the composites, resulting in the increase of conductivity and the decrease of R_{ct}.[23] The as-prepared composite in this study was found to have an ultra-low R_{ct} (0.001 Ω) without the addition of a binder and a conductive agent.

Moreover, the Ni₃S₂/MnS/CuS/@rGO-NF and rGO-NF were selected as electrodes to build asymmetric supercapacitor. Generally, the asymmetric supercapacitor consists of a battery-type electrode (tantalum capacitor) and a capacitor-type electrode (electrochemical double layer), exhibiting better reversibility, high energy density, and power density.[24,25] Depending on the electrolyte, asymmetric supercapacitors are classified into two types, non-aqueous and aqueous. Non-aqueous electrolytes have slow insertion kinetics, resulting in moderate decoupling power delivery performance and greatly reduced energy density due to the low viscosity and high pH value of the aqueous electrolyte. However, ion mobility is an essential prerequisite for rapid reaction kinetics. Therefore, aqueous electrolytes got more and more attention. Currently, CuS‖AC-ASC,[26] ZNACOs‖AC,[27] ZnFe₂O₄‖Ni(OH)₂ (ref. 28) and CoFe₂O₄-‖rGO under aqueous electrolytes have been reported,[29] their specific capacitance reached 48.2 F g⁻¹, 232 F g⁻¹, 118 F g⁻¹ and 38 F g⁻¹. In contrast, the Ni₃S₂/MnS/CuS/@rGO-NF‖rGO-NF asymmetric supercapacitor exhibited a high specific capacitance of 522 F g⁻¹ at 2 A g⁻¹.

Experimental part

Materials and reagents. Graphite powder (purity 99%) was provided by Tian City Kermel Chemical Reagent (China), H₂SO₄ (98.08%), NaNO₃ and HCl (36%) were purchased from Tianjin city Kermel Chemical Reagent (China). MnCl₂·4H₂O and H₂O₂ (30%, 500 ml) were purchased from Tianjin Kaitong Chemical Reagent Co., Ltd. NiCl₂·6H₂O (AR) were purchased from Tianjin Dongli District Tianda Chemical Reagent Factory. CuCl₂·2H₂O (AR) was ordered from Tianjin Komiou Chemical Reagent Co., Ltd. CH₄N₂S (Tu) (AR) was ordered from Henan Dongyang Chemical Products Co., Ltd. KMnO₄ was ordered from National Group Chemical Reagent Co., Ltd. Nickel foam (NF) was ordered from Kunshan Yujiaxin Electronic Technology Co., Ltd. DMF (AR) was ordered from Tianjin Tianli Chemical Reagent Co., Ltd. Ethylene glycol (AR) was purchased from Tianjin Hongyan Reagent Factory. Ultra-purified (UP) water with resistivity of 18.2 MΩ cm was used throughout the experiment.

Preparation of GO. Graphite oxide (GO) was prepared by the modified Hummers' method.[15] Typically, 5 g graphite power and 2.5 g sodium nitrate (NaNO₃) were added to 115 ml of concentrated sulfuric, the reaction was kept in the ice bath for 30 min at 5 °C. Then 15 g KMnO₄ was introduced, followed by a reaction at 35 °C for 30 min. Afterwards, 230 ml of water was added dropwise into the suspension, and the obtained suspension was heated up to 98 °C. After 15 min, the suspension was further diluted to 420 ml and treated by 50 ml 30 wt% hydrogen peroxide. The graphite oxide (GO) was thereby obtained after repeated centrifugation, washing, and drying.

Nickel foam pretreatment. The nickel foam (NF) was placed into a rectangular plate of dimension 100 mm × 100 mm × 1 mm, followed by ultrasonic treatment with HCl. Then NF was washed with acetone and deionized water for four times at a frequency of 100 Hz to remove the oxides on the NF surface. Afterwards, NF was dried in the vacuum oven under 70 °C for 12 h, and cut into a size of 10 mm × 10 mm × 1 mm for utilization.

Synthesis of Ni₃S₂/MnS/CuS@rGO-NF nanocomposites. NiCl₂·6H₂O (1 mmol), MnCl₂·4H₂O (1 mmol), CuCl₂·2H₂O (1 mmol), Tu (8 mmol) were dissolved in 40 ml of anhydrous N,N-
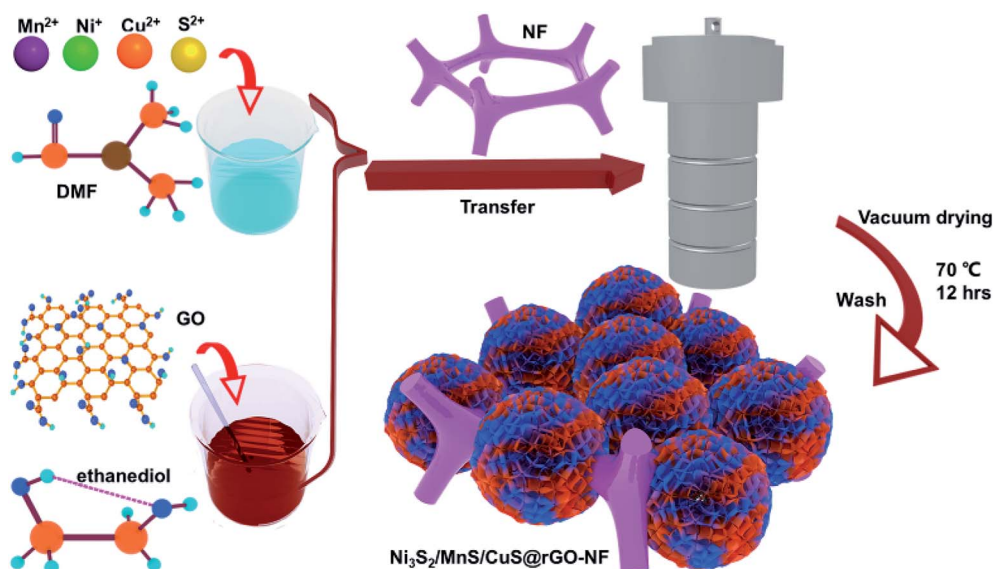
Fig. 1 Schematical fabrication of Ni₃S₂/MnS/CuS@rGO-NF nanocomposites.
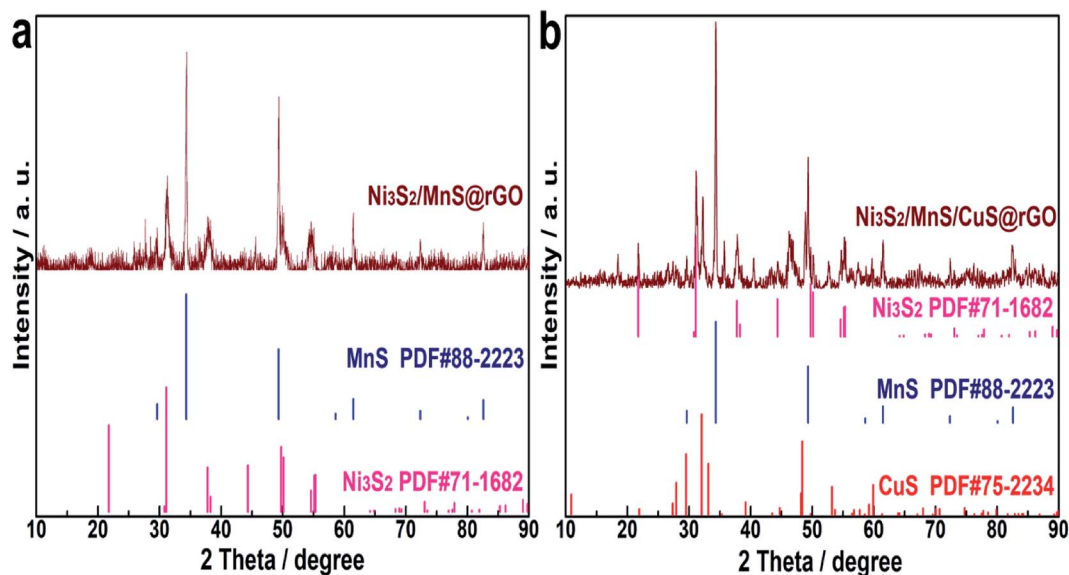
Fig. 2 XRD patterns of (a) Ni₃S₂/MnS@rGO and (b) Ni₃S₂/MnS/CuS@rGO.

dimethylformamide (DMF) by sonication. Then, 0.5 mg ml⁻¹ GO dispersion was prepared by dispersing 20 mg GO in 40 ml of ethylene glycol. Afterwards, the pretreated NF was blended with the above-mentioned solutions and transferred into a 100 ml Teflon-lined autoclave vessel and the reaction was remained at 180 °C for 24 h. The Ni₃S₂/MnS/CuS@rGO-NF composites were thereby obtained. Ni₃S₂/MnS/CuS@rGO was also prepared

without the addition of NF based on the above experimental procedure. The as-prepared Ni₃S₂/MnS/CuS@rGO-NF and Ni₃S₂/MnS/CuS@rGO were washed with deionized water and ethanol for three times respectively and then dried in a vacuum oven at 70 °C for 12 h. The preparation scheme of Ni₃S₂/MnS/CuS@rGO is shown in Fig. 1.
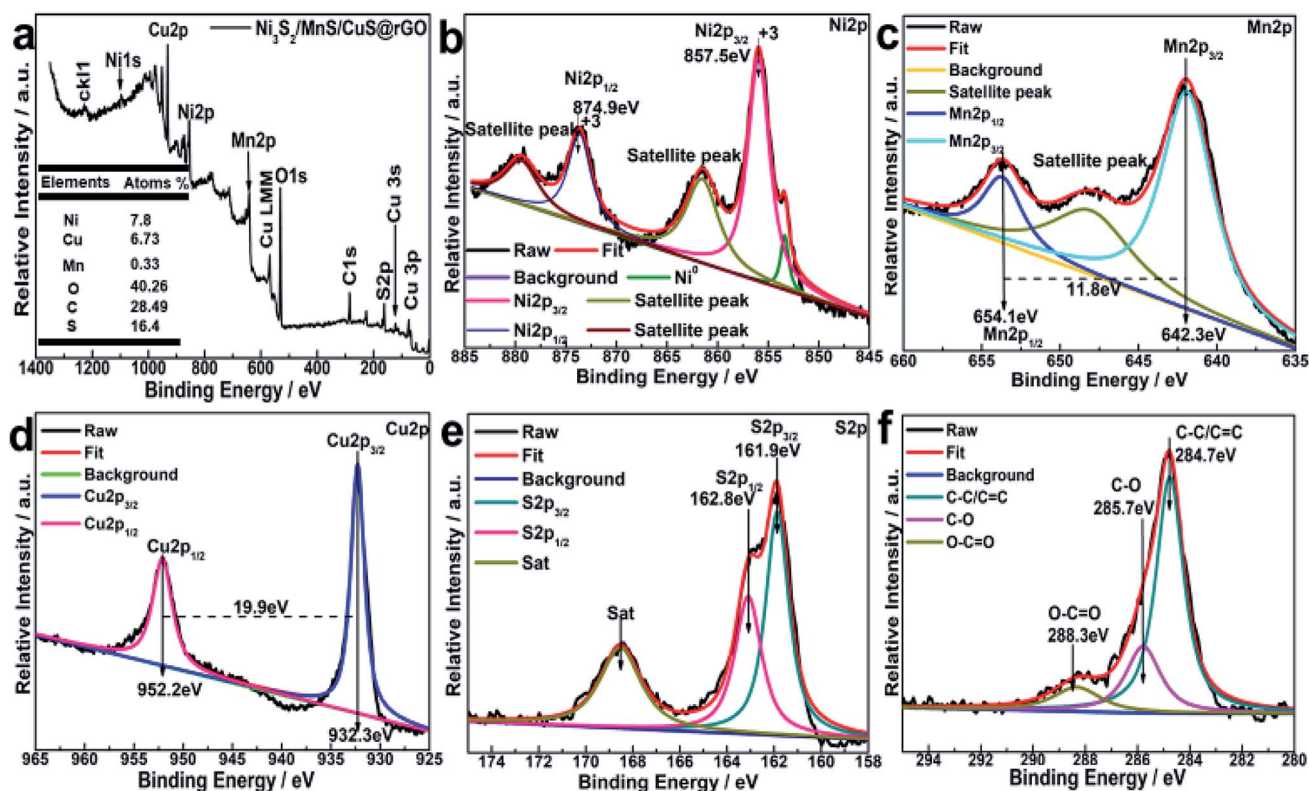
Fig. 3 X-ray photoelectron spectra of N₃S₂/MnS/CuS@rGO: (a) survey spectrum, (b) Ni 2p spectrum, (c) Mn 2p spectrum, (d) Cu 2p spectrum, (e) S 2p spectrum and (f) high-resolution C 1s spectrum respectively.
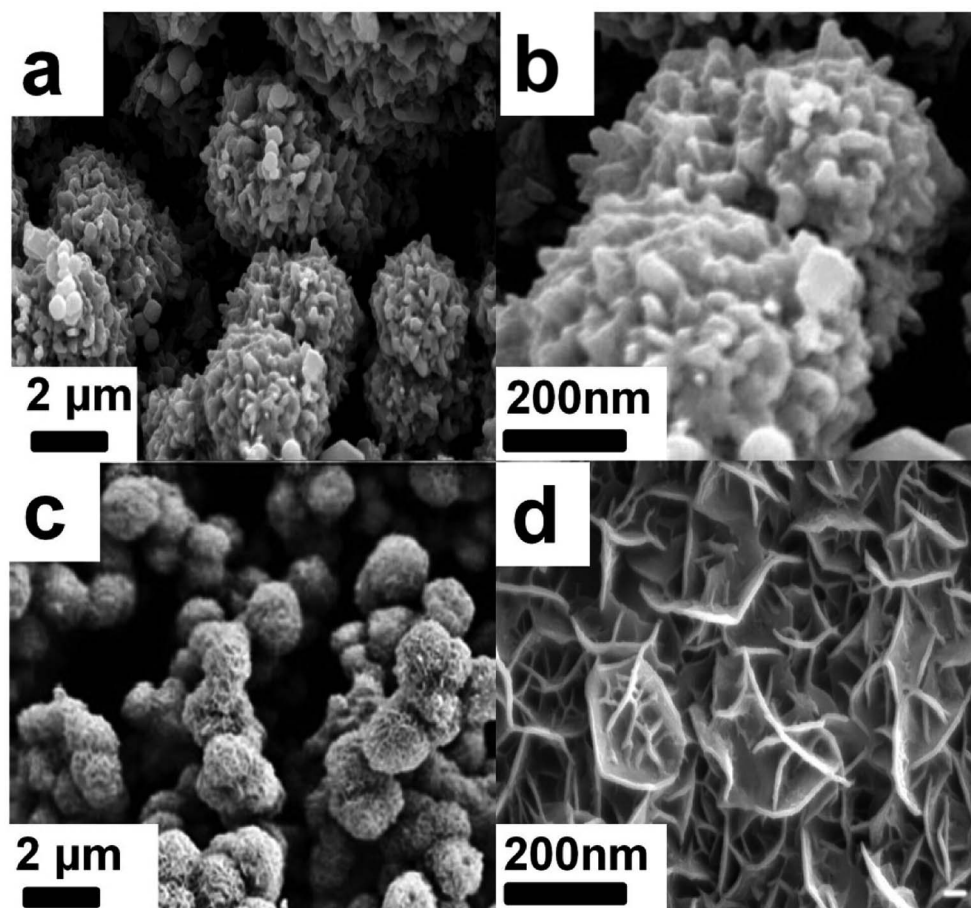
Fig. 4 Morphology of Ni$_3$S$_2$/MnS/CuS@rGO at low magnification (a) and high magnification (b); morphology of Ni$_3$S$_2$/MnS/CuS at low magnification (c) and high magnification (d).

Assembly of the asymmetric supercapacitor. In order to evaluate the Ni$_3$S$_2$/MnS/CuS@rGO composite electrode for practical application, asymmetric supercapacitor (ASC) was assembled with Ni$_3$S$_2$/MnS/CuS@rGO-NF as positive electrode (PE), graphene-loaded Ni foam as negative electrode (NE), 6 M KOH solution as electrolyte, and cellulose paper as separator.[30] During the preparation of PE and NE, 2 ml PVDF (0.025 g ml^{-1}) was utilized as binder and 0.05 g of acetylene black was adopted as conductive agent.

Characterization. The phase information was obtained by an X-ray diffraction spectrometer (XRD, TTR-III, Rigaku, Japan) equipped with Cu target radiation. Elemental analysis was performed on an X-ray photoelectron spectrometer (XPS, KRATOS XSAM 800, United Kingdom) equipped with Mg Kα X-ray radiation. The morphology and structure were elucidated by scanning electron microscope (SEM, JSM-6360, JEOL, Japan), transmission electron microscope (TEM, TECHNI-G2, FEI, US), energy dispersive X-ray spectroscopy (EDS, JEOL, JEM-2100F, Japan) and the high-resolution TEM (HRTEM, JEM-2100F, JEOL, Japan).

Electrochemical measurements. Electrochemical measurements for electrodes were taken using a half-cell three-electrode system on electrochemical work station (CHI660E,

Shanghai Chenhua Corp. China) at room temperatures (25 °C), using saturated calomel electrode (SCE) as reference electrode, 1 cm × 1 cm platinum plate as counter electrode, 6 M KOH aqueous electrolyte as electrolyte and Ni$_3$S$_2$/MnS/CuS@rGO-NF as working electrode. Cyclic voltammetry (CV) and galvanostatic charge/discharge (GCD) experimental analysis were performed under various scan rates and current densities with a potential window from −0.3 to 0.4 V. The electrochemical impedance spectroscopy (EIS) plots were recorded in frequency width of 0.01 Hz to 100 kHz with an ac voltage of 5.0 mV. The mass specific capacitance (C_m) is calculated based on eqn (1):

$$C_m = \frac{I \times \Delta t}{m \times \Delta V} \tag{1}$$

where I is the discharge current, Δt is the discharge time (s), m is the mass (g) of the active material in the electrode, and ΔV is the voltage window (V).

The energy density (E, W h kg^{-1}) and power density (P, W kg^{-1}) of electrode were calculated according to eqn (2) and (3):[31,32]

$$E = \frac{C(\Delta V)^2 \times 1000}{2 \times 3600} \tag{2}$$

$$P = \frac{E}{\Delta t} \times 3600 \qquad (3)$$

where ΔV is the potential window (V), C is the specific capacity ($F\ g^{-1}$), and Δt is the discharge time (s).

Electrochemical measurements such as CV, GCD and EIS for asymmetric supercapacitor were also carried out on electrochemical work station (CHI660E, Shanghai Chenhua Corp. China) at room temperatures (25 °C) using four-electrode system. CV and GCD analysis were performed under various scan rates and current densities with a potential window from 0 to 1.5 V. The EIS plots were recorded in frequency width of 0.01 Hz to 100 kHz with an ac voltage of 5.0 mV.

The energy density (E, W h kg^{-1}) and power density (P, W kg^{-1}) of the battery are calculated from the discharge curve according to the following equation:

$$E = C_m(\Delta V)^2/8 \qquad (4)$$

$$P = E/\Delta t \qquad (5)$$

where C_m, ΔV, and Δt are the mass-specific capacitance, cell voltage (1.5 V), and discharge time, respectively.

Results and discussion

Phase and elemental analysis

XRD patterns of $Ni_3S_2/MnS@rGO$ and $Ni_3S_2/MnS/CuS@rGO$ are shown in Fig. 2a and b, respectively. By comparison of Fig. 2a and b, the introduction of Cu^{2+} ions did not change the structural phase of Ni^+ and Mn^{2+}. The characteristic diffraction peaks of r-MnS are detected at 29.62°, 34.62°, 49.34°, 58.60°, 61.48°, 72.35°, 80.06°, 82.59°, which correspond to the (111), (200), (220), (311), (222), (400), (331), (420) of r-MnS (JCPDS, PDF no: 64-3413). The diffraction peaks at $2\theta = 21.76°$, 31.10°, 37.80°, 44.35°, 49.73°, 50.11°, 54.61° and 55.16° correspond to (010), (−110), (111), (020), (120), (−120), (121) and (−121) crystal planes in Ni_3S_2 (JCPDS-no. 44-1418).[33] The diffraction peaks at 2θ values of 27.37°, 29.54°, 32.07°, 33.13° in Fig. 2b are attributed to the (100), (102), (103) and (006) crystal planes of CuS phase (JCPDS, PDF no. 06-0464).[10]

For determining the chemical state and electronic states of the elements on the surface $Ni_3S_2/MnS/CuS@rGO$ composites, XPS analysis is conducted, as shown in Fig. 3. The XPS survey spectrum confirms the coexistence of Ni, Cu, Mn, O, C and S (Fig. 3a). The contents of Ni, Cu, Mn, O, C and S elements are calculated to be 7.8 at%, 6.73 at%, 0.33 at%, 40.26 at%, 28.49 at% and 16.4 at%, respectively. The characteristic peak at 569.08 eV for Cu LMM is the typical binding energy value for CuS (Fig. 3a), corroborating that Cu element is existent in the form of bivalent state.

The Ni 2p spectrum is deconvoluted into two spin–orbit bimodal peaks of Ni^{2+} and Ni^{3+} and two shake-up satellite peaks (Fig. 3b).[20] The characteristic peaks at 857.5 eV and 874.9 eV are assigned to Ni $2p_{3/2}$ and Ni $2p_{1/2}$, respectively. The binding energy difference of Ni $2p_{3/2}$ and Ni $2p_{1/2}$ is 17.4 eV, indicating the co-existence of di/tri-valent state.
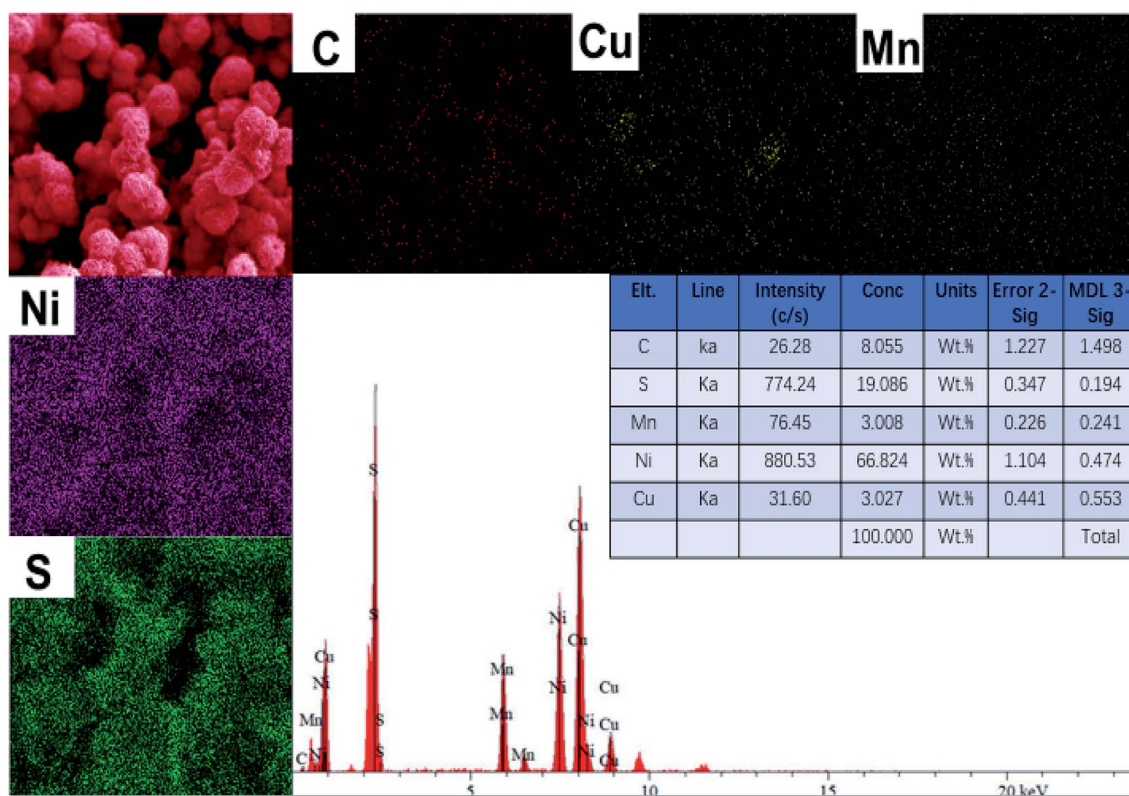

Elt.	Line	Intensity (c/s)	Conc	Units	Error 2-Sig	MDL 3-Sig
C	ka	26.28	8.055	Wt.%	1.227	1.498
S	Ka	774.24	19.086	Wt.%	0.347	0.194
Mn	Ka	76.45	3.008	Wt.%	0.226	0.241
Ni	Ka	880.53	66.824	Wt.%	1.104	0.474
Cu	Ka	31.60	3.027	Wt.%	0.441	0.553
			100.000	Wt.%		Total

Fig. 5 The EDS spectra of C, Cu, Mn, Ni and S on spherical $Ni_3S_2/MnS/CuS@rGO$ nanostructures.
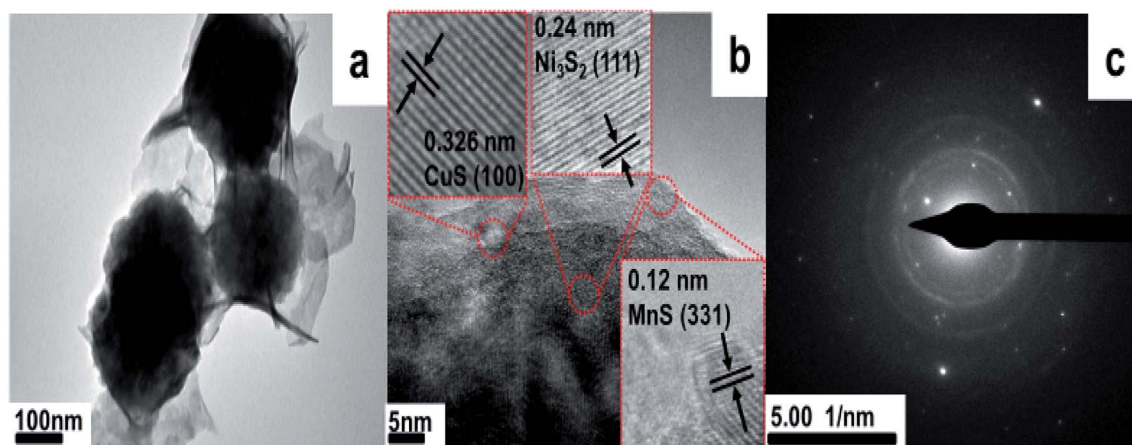
Fig. 6 (a) TEM of $Ni_3S_2/MnS/CuS@rGO$, and (b) the HRTEM of $Ni_3S_2/MnS/CuS@rGO$. (c) Selected-area electron diffraction (SAED) pattern of $Ni_3S_2/MnS/CuS@rGO$.

The Mn peaks in Fig. 3c are observed in the range of 635.0–655 eV. Mn $2p_{3/2}$ and Mn $2p_{1/2}$ peaks at 642.3 eV and 654.1 eV with the spin energy separation of ~11.8 eV, indicate the presence of Mn^{2+} oxidation (Fig. 3d).[34] Two peaks at 932.3 and 952.2 eV are due to Cu $2p_{3/2}$ and Cu $2p_{1/2}$.[35] The peaks at 161.9 eV and 162.8 eV are associated with S $2p_{3/2}$ and S $2p_{1/2}$ in the metal sulfide. The peak at 168.6 eV could be ascribed to sulfur in oxidation state (Fig. 3f).[36] C 1s peak can be fitted into three Gaussian peaks centered at 284.6 eV, 286.0 eV and 288.6 eV, which are attributed to C=C, alkyl C–C, and O=C–O, respectively.[36–39]
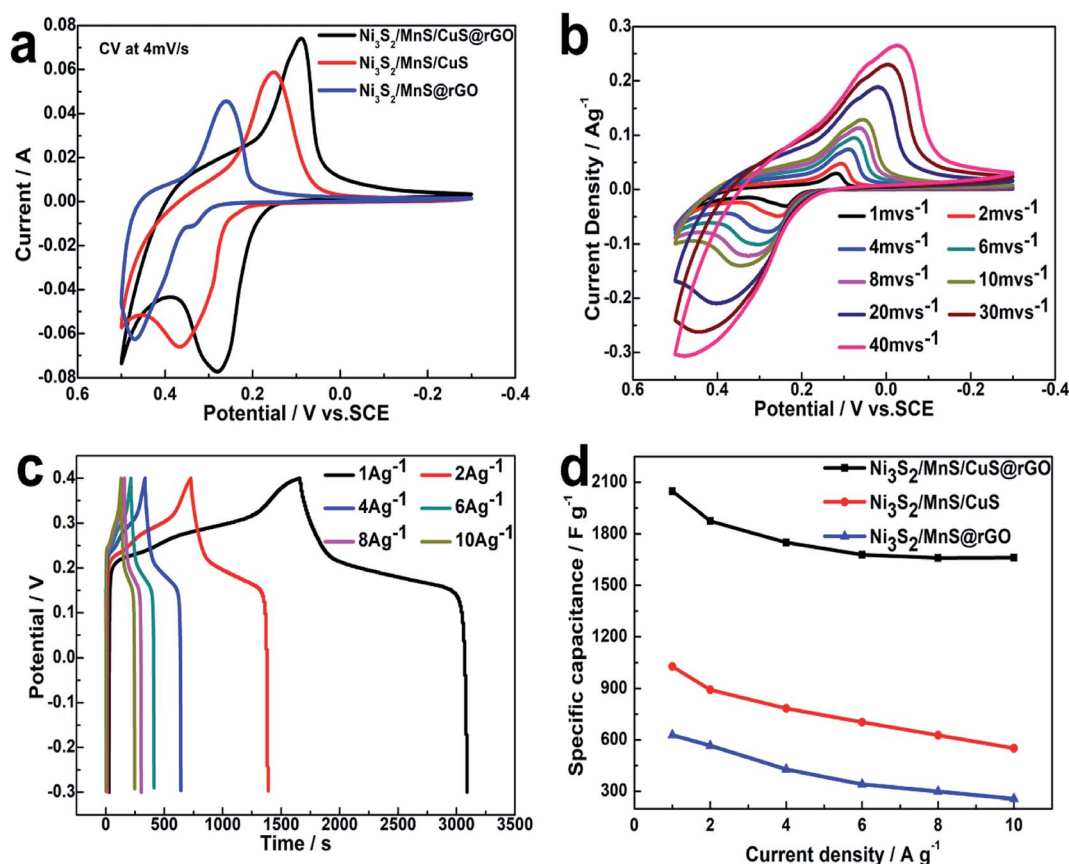

Fig. 7 (a) CV plots of $Ni_3S_2/MnS/CuS@rGO$, $Ni_3S_2/MnS/CuS$ at a 4 mV s^{-1}. (b) CV plots of $Ni_3S_2/MnS/CuS@rGO$ composites at various voltage sweeps (1, 2, 4, 6, 8, 10, 20, 30, 40 mV s^{-1}) in 6.0 M KOH. (c) GCD analyses of $Ni_3S_2/MnS/CuS@rGO$ composites at various current densities (1, 2, 4, 6, 8 and 10 A g^{-1}). (d) Specific capacitance of $Ni_3S_2/MnS/CuS@rGO$, $Ni_3S_2/MnS/CuS$ composites at different current densities (1, 2, 4, 6, 8 and 10 A g^{-1}) in 6.0 M KOH.

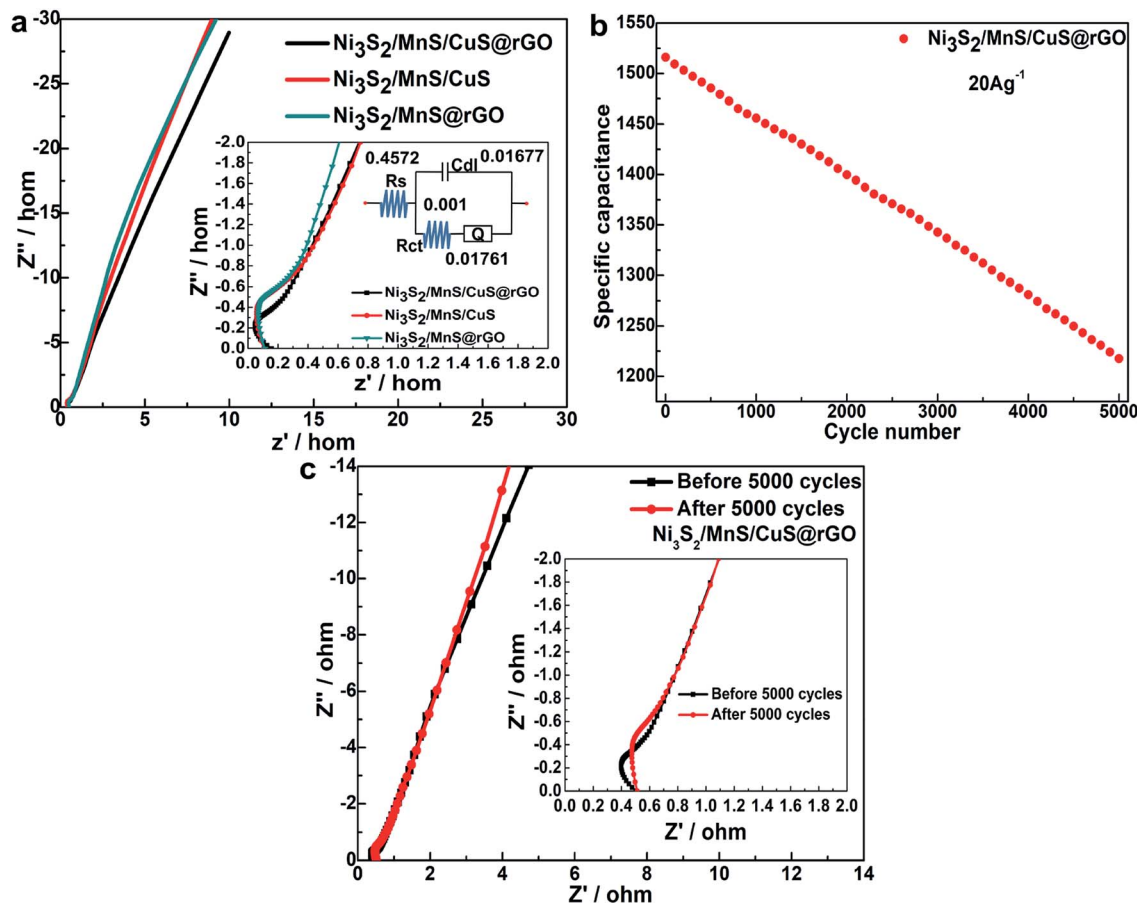**Fig. 8** (a) Nyquist plots of the $Ni_3S_2/MnS/CuS@rGO$, $Ni_3S_2/MnS/CuS$ composites electrodes in 6.0 M KOH in the frequency width from 0.01 to 100 kHz. (b) Cyclic performance of the $Ni_3S_2/MnS/CuS@rGO$ electrodes at 20 A g^{-1} in 6.0 M KOH (aq). (c) Nyquist plots of $Ni_3S_2-MnS-CuS@rGO$ before and after 5000 cycles.

Morphology analysis

The SEM morphology of $Ni_3S_2/MnS/CuS@rGO$ and $Ni_3S_2/MnS/CuS$ are provided, as shown in Fig. 4. Without the addition of rGO, $Ni_3S_2/MnS/CuS$ displays spherical morphology assembled by closely packed nanosheets (Fig. 4a and b). With the incorporation of rGO template, $Ni_3S_2/MnS/CuS@rGO$ also shows spherical morphology with much lower diameter. rGO nanosheets can functionalize as template to induce the growth of $Ni_3S_2/MnS/CuS$, forming a three-dimensional porous spherical structure self-assembled by nanosheets (Fig. 4c and d), generating a more efficient electron transport structure. EDS spectra of $Ni_3S_2/MnS/CuS@rGO$ composite certify the presence of C, Ni, Mn, Cu and S elements (Fig. 5), confirming the successful fabrication of the $Ni_3S_2/MnS/CuS@rGO$ composite.

TEM and HRTEM morphology of $Ni_3S_2/MnS/CuS@rGO$ is further offered, as shown in Fig. 6. Spherical morphology is also observed for $Ni_3S_2/MnS/CuS@rGO$. HRTEM images (Fig. 6b) show clear fringes with a measured interplanar spacing of 0.326 nm, 0.24 nm and 0.12 nm that correspond to CuS (100), Ni_3S_2 (111) and MnS (331), respectively, which is in good agreement with the XRD results. The SAED pattern (Fig. 6c) shows a concentric diffraction ring, demonstrating the existence of polycrystalline structure.
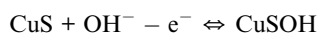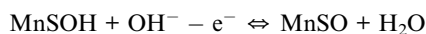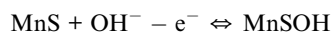
Electrochemical analysis of electrodes

CV curves of $Ni_3S_2/MnS/CuS@rGO$, $Ni_3S_2/MnS@rGO$ and $Ni_3S_2/MnS/CuS$ composite electrodes are compared at 4 mV s^{-1} with a potential window from −0.3 to 0.4 V, as shown in Fig. 7a. All CV curves show a pair of strong redox peaks, demonstrating that the $Ni_3S_2/MnS/CuS@rGO$ electrode presents pseudocapacitance behavior, as shown in Fig. 7a. $Ni_3S_2/MnS/CuS@rGO$ displays more intense current density than $Ni_3S_2/MnS/CuS@rGO$ and $Ni_3S_2/MnS@rGO$, suggesting enhanced activity and specific capacitance.[37]

As shown in Fig. 7b, the redox peak in the CV curve may be correlated with the redox reaction between M^{2+} and M^{3+} (M represents Ni, Cu and Mn elements), as expressed by eqn (6)–(9).[40–42] The peaks are located at 0.12 V and 0.32 V when the scan rate is 2 mV s^{-1}. With the 20-fold increase in the scan rate from 2 to 40 mV s^{-1}, the position of the cathodic peak shifts from 0.12 V to −0.02 V, suggesting the lower resistance of the electrode.[3] Moreover, almost no deformation takes place in the CV peak shape as the scan rate increases, certifying rapid electron transport and charge separation.

$$Ni_3S_2 + 3OH^- - 3e^- \Leftrightarrow Ni_3S_2(OH)_3 \qquad (6)$$

Table 1 Comparison analysis of electrochemical properties of Ni_3S_2/MnS/CuS@rGO in three-electrode system

Electrode materials	Specific capacitance		Capacity retention	R_s	R_{ct}	Reference
	Low current density	High current density				
Ni_3S_2	—	—	—	0.72	0.26	37
Ni_3S_2@rGO	—	—	—	0.37	0.29	37
a-MnS/N-rGO	933.6 F g^{-1} at 1 A g^{-1}	469.1 F g^{-1} at 20 A g^{-1}	70% after 2000 cycles at 10 A g^{-1}	0.78	3.7	18
The γ-MnS/rGO-60 composite	547.6 F g^{-1} at 1 A g^{-1}	351.4 F g^{-1} at 20 A g^{-1}	70% after 3000 cycles at 5 A g^{-1}	1.1	0.20	14
MnS/Ni_xS_y	1073.81 F g^{-1} at 1 A g^{-1}	428.57 F g^{-1} at 20 A g^{-1}	89% after 10 000 cycles at 6 A g^{-1}	0.25	0.52	48
$CoNi_2S_4$/CNLDHs	1027 F g^{-1} at 0.5 A g^{-1}	600 F g^{-1} at 10 A g^{-1}	Decreased ~18% after 2000 cycles at 10 A g^{-1}	—	0.35	46
$CoNi_2S_4$/RGO	1706 F g^{-1} at 0.5 A g^{-1}	1268 F g^{-1} at 10 A g^{-1}	Decreased ~8% after 2000 cycles at 10 A g^{-1}	—	0.20	46
$Ni_{0.67}Cu_{0.33}Co_2S_4$	1341 F g^{-1} at 1 A g^{-1}	1078 F g^{-1} at 10 A g^{-1}	71.7% after 10 000 cycles at 4 A g^{-1}	0.33	0.08	47
CZTS/RGO	591 F g^{-1} at 0.25 A g^{-1}	—	80.6% after 1000 cycles at 1 A g^{-1}	0.51	0.04	48
Ni_3S_2/MnS/CuS@rGO	2042 F g^{-1} at 1 A g^{-1}	1655 F g^{-1} at 10 A g^{-1}	78.3% after 5000 cycles at 20A g^{-1}		0.46	0.001	This work

$$MnS + OH^- - e^- \Leftrightarrow MnSOH \quad (7)$$

$$MnSOH + OH^- - e^- \Leftrightarrow MnSO + H_2O \quad (8)$$

$$CuS + OH^- - e^- \Leftrightarrow CuSOH \quad (9)$$

Fig. 7c shows the galvanostatic charge–discharge curves for the Ni_3S_2/MnS/CuS@rGO electrode at various current densities in the range of −0.3 V to 0.4 V. A plateau is distinctly observed in the discharge curves due to the electrochemical and concentration polarizations.[20] At a current density of 1 A g^{-1}, the specific capacitance is 1028 F g^{-1} for Ni_3S_2/MnS/CuS, 628.6 F g^{-1} for Ni_3S_2/MnS@rGO, and 2042 F g^{-1} for Ni_3S_2/MnS/

CuS@rGO, respectively. Ni_3S_2/MnS/CuS@rGO shows better stability and higher specific capacitance than Ni_3S_2/MnS/CuS and Ni_3S_2/MnS@rGO at various current densities (Fig. 7d). These data show that the electrochemical performances of Ni_3S_2/MnS/CuS@rGO have been enhanced due to the intervention of Cu^{2+} and graphene.

The Nyquist plots of the Ni_3S_2/MnS/CuS/@rGO, Ni_3S_2/MnS/CuS and Ni_3S_2/MnS@rGO electrodes are obtained by electrode impedance spectroscopy (EIS), as shown in Fig. 8a. Ni_3S_2/MnS/CuS@rGO exhibits smaller charge transfer resistance (R_{ct}). The R_{ct} of Ni_3S_2/MnS/CuS@rGO (0.001 Ω) is much lower than that of Ni_3S_2/MnS@rGO by 0.02 Ω, and lower than that of Ni_3S_2/MnS/CuS by 0.017 Ω, which can be ascribed to the high
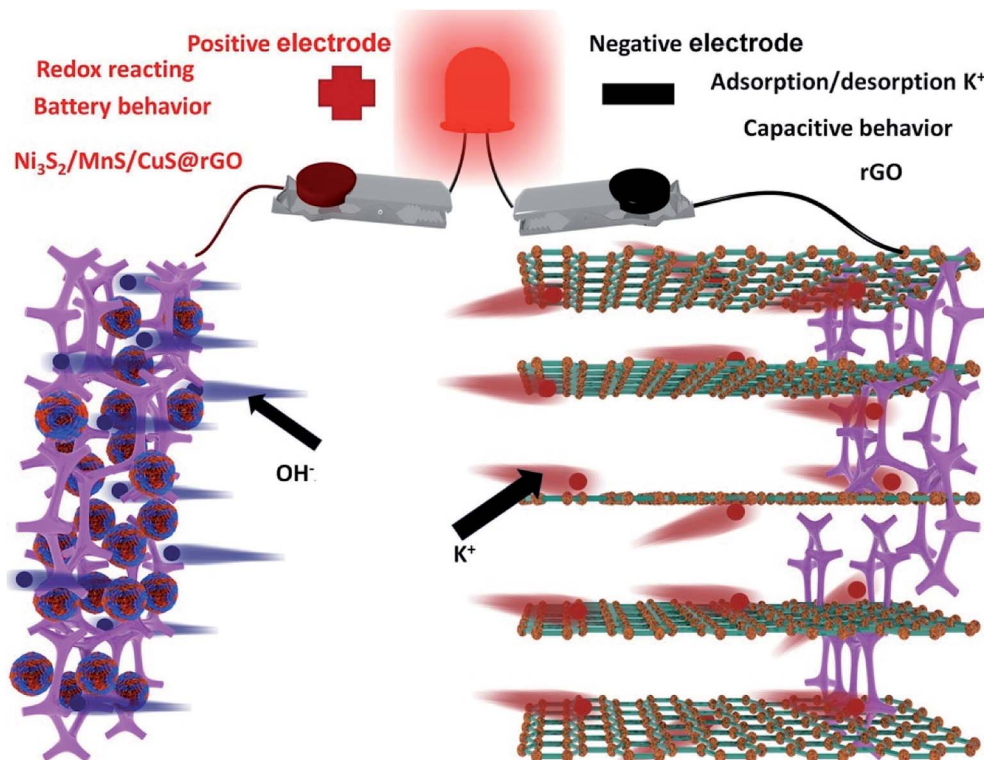
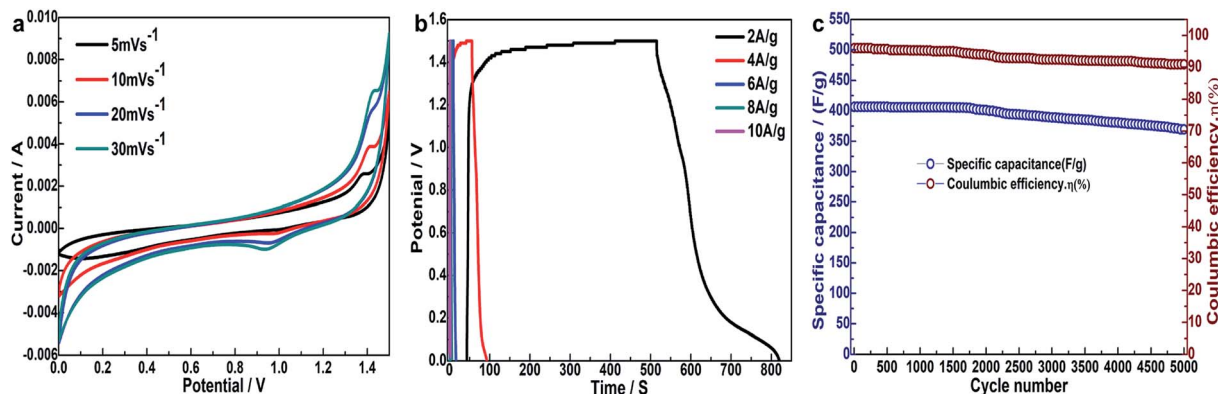**Fig. 9** 3D model diagram of the Ni_3S_2/MnS/CuS@rGO‖rGO asymmetric supercapacitor.

Fig. 10 (a) CV curves of Ni_3S_2/MnS/CuS@rGO supercapacitor for battery mixers. (b) GCD curves at different current densities. (c) Specific capacitance and coulombic efficiency (η) of the ASC equipment.

electroconductivity of active materials and the structure of active materials.[43] After 5000 cycles, Ni_3S_2–MnS–CuS@RGO electrode maintains 78.3% of the initial capacity. This indicates that the (Ni_3S_2/MnS/CuS@rGO)/NF asymmetric electrode exhibits good capacitance retention at 20 A g^{-1} (Fig. 8b). Fig. 8c shows the Nyquist plots of Ni_3S_2/MnS/CuS@rGO electrode at 0.3 V bias potential before and after 5000 GCDs. R_{ct} only increases by 0.024 Ω after the 5000 cycles, proving that Ni_3S_2/MnS/CuS@rGO has high durability and electrochemical stability even after long-term cycling.

The electrochemical properties of Ni_3S_2/MnS/CuS@rGO electrode are also compared with those electrodes reported in the literatures, as listed in Table 1. It demonstrates that the Ni_3S_2/MnS/CuS@rGO electrode is endowed with excellent specific capacitance and capacity, as well as low R_{ct}.

Electrochemical analysis of asymmetric supercapacitor

The 3D schematic model and energy storage mechanism of asymmetric supercapacitor is illustrated in Fig. 9, which use Ni_3S_2/MnS/CuS@rGO as the positive electrode, rGO as the negative electrode and 6 M KOH as electrolyte. In battery dynamics, the charge storage process of two ions is faster than that of single ion shuttle reaction. Therefore, hybrid battery power equipment such as asymmetric supercapacitor is able to achieve higher energy and higher power performance. As shown in the 3D schematic model, K^+ and OH^- ions move towards the negative and positive electrodes during the process of charge–discharge process. The cell works by redox reactions with OH^- on the Ni_3S_2/MnS/CuS@rGO positive electrode and simultaneous adsorption/desorption of K^+ cations on the rGO negative electrode [44].
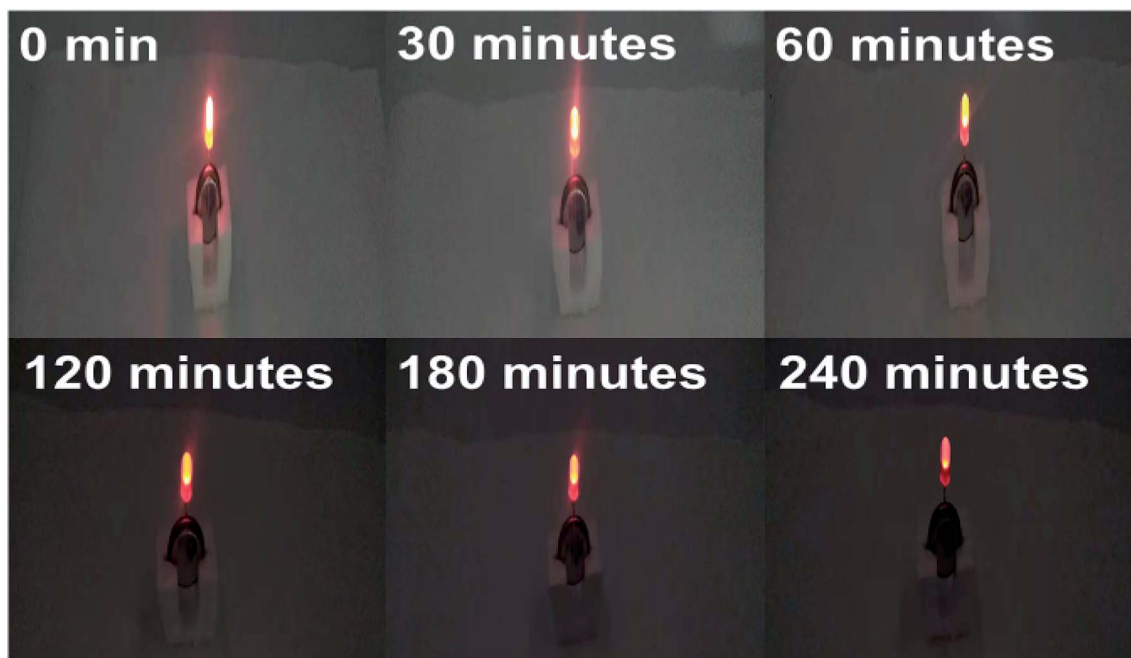

Fig. 11 The button batteries supplied power for a red LED indicator for 240 min.

The Ni$_3$S$_2$/MnS/CuS@rGO asymmetric supercapacitor devices exhibit some excellent electrochemical performances on the basis of CV curves at various voltage sweeps and GCD current at various densities (Fig. 10a and b). Fig. 10a shows the CV cures of the ASC plotted in the potential window of 0 V to 1.5 V at varying scan rates (5–30 mV s^{-1}). All the CV plots are similar in shape, maintaining a pair of cathodic and anodic peaks. The redox peaks in the CV plots are found to shift away from each other with increasing scan rates. The redox peaks are indicative of the pseudocapacitive nature of ASC, which is clear from the large area of the corresponding CV plots.[25] The specific capacity is calculated by using the net mass of Ni$_3$S$_2$/CuS@rGO electroactive material. Hybrid power supply devices provide a specific capacitance of 522.2 F g^{-1} at 2A g^{-1}.

After 5000 GCD cycles, the specific capacity of asymmetric batteries is maintained at 90.8% of the initial state (Fig. 10c), exhibiting excellent cycle stability. A simple application to power a red commercial light-emitting diode (LED) is conducted (Fig. 11). The asymmetric supercapacitor device is able to power a red LED indicator for 240 min.

Conclusions

Ternary Ni$_3$S$_2$/MnS/CuS composites were successfully fabricated on nickel foam *via* electrostatic adsorption of Ni$^+$, Mn^{2+} and Cu^{2+} ions on rGO nanosheet template based on hydrothermal method. The chemical structure was certified by XRD, XPS, SEM and HRTEM. Ni$_3$S$_2$/MnS/CuS displayed spherical morphology assembled by closely packed nanosheets, while Ni$_3$S$_2$/MnS/CuS@rGO showed 3D porous spherical morphology with much lower diameter, generating a more efficient electron transport structure. Ni$_3$S$_2$/MnS/CuS@rGO was demonstrated to have better stability and higher specific capacity than Ni$_3$S$_2$/MnS/CuS, and Ni$_3$S$_2$/MnS@rGO at various current densities. The R_{ct} of Ni$_3$S$_2$/MnS/CuS@rGO was also much lower owing to the high electroconductivity of active materials and the unique structure of active materials. The electrochemical performances of Ni$_3$S$_2$/MnS/CuS@rGO electrode have been significantly improved due to the intervention of Cu^{2+} and graphene. The asymmetric supercapacitor assembled with Ni$_3$S$_2$/MnS/CuS@rGO as positive electrode and rGO as negative electrode also presented excellent cycle stability. Ni$_3$S$_2$/MnS/CuS@rGO will have promising applications in the field of energy storage devices.

Conflicts of interest

There are no conflicts to declare.

Acknowledgements

Notes and references

1 P. J. Hall and E. J. Bain, *Energy Policy*, 2008, **36**, 4352–4355.
2 Q. Wang, J. Yan and Z. Fan, *Energy Environ. Sci.*, 2016, **9**, 729–762.
3 G. Zhang, H. Wu, H. E. Hoster, M. B. Chan-Park and X. Lou, *Energy Environ. Sci.*, 2012, **5**, 9453–9456.
4 Z. Chen, J. Wen, C. Yan, L. Rice, H. Sohn, M. Shen, M. Cai, B. Dunn and Y. Lu, *Adv. Energy Mater.*, 2011, **1**, 551–556.
5 C. Yuan, J. Li, L. Hou, X. Zhang, L. Shen and X. Lou, *Adv. Funct. Mater.*, 2012, **22**, 4592–4597.
6 P. Simon and Y. Gogtsi, *Nat. Mater.*, 2008, **7**, 845–854.
7 P. Himasree, I. K. Durga, T. N. V. Krishna, S. S. Rao, C. V. V. M. Gopi, S. Revathi, K. Prabakar and H. Kim, *Electrochim. Acta*, 2019, **305**, 467–473.
8 Y. Huang, T. Shi, Y. Zhong, S. Cheng, S. Jiang, C. Chen, G. Liao and Z. Tang, *Electrochim. Acta*, 2018, **269**, 45–54.
9 W. Zhou, X. Cao, Z. Zeng, W. Shi, Y. Zhu, Q. Yan, H. Liu, J. Wang and H. Zhang, *Energy Environ. Sci.*, 2013, **6**, 2216–2221.
10 S. Tang, B. Zhu, X. Shi, J. Wa and X. Meng, *Adv. Energy Mater.*, 2017, **7**, 1601985–1601996.
11 J. Zhu, S. Tang, J. Wu, X. Shi, B. Zhu and X. Meng, *Adv. Energy Mater.*, 2017, **7**, 1601234–1601245.
12 J. Yang, C. Yu, X. Fan, S. Liang, S. Li, H. Huang, Z. Ling, C. Hao and J. Qiu, *Energy Environ. Sci.*, 2016, **9**, 1299–1307.
13 W. Liu, H. Niu, J. Yang, K. Cheng, K. Ye, K. Zhu, G. Wang, D. Cao and J. Yan, *Chem. Mater.*, 2018, **30**, 1055–1068.
14 G. Zhao, M. Kong, Y. Yao, L. Long, M. Yan, X. Liao, G. Yin, Z. Huang, A. M. Asiri and X. Sun, *Nanotechnology*, 2017, **28**, 065402–065414.
15 Y. Ren, J. Wang, X. Huang and J. Ding, *Solid State Ionics*, 2015, **278**, 138–143.
16 C. Dai, P. Chem, J. Lin, S. Chou, W. Wu, P. Li, K. Wu and T. Lin, *ACS Appl. Mater. Interfaces*, 2013, **5**, 12168–12174.
17 Z. Li, B. Li, C. Liao, Z. Liu, D. Li, H. Wang and Q. Li, *Electrochim. Acta*, 2017, **253**, 344–356.
18 H. Quan, B. Cheng, D. Chen, X. Su, Y. Xiao and S. Lei, *Electrochim. Acta*, 2016, **210**, 557–566.
19 X. Huang, Z. Zhang, H. Li, Y. Zhao, H. Wang and T. Ma, *J. Alloys Compd.*, 2017, **72**, 2662–2668.
20 Z. Zhang, X. Huang, H. Li, Y. Zhao and T. Ma, *Appl. Surf. Sci.*, 2017, **400**, 238–244.
21 A. Wang, H. Wang, S. Zhang, C. Mao, J. Song, H. Niu, B. Jin and Y. Tian, *Appl. Surf. Sci.*, 2013, **282**, 704–708.
22 H. Liu, Z. Guo, X. Wang, J. Hao and J. Lian, *Electrochim. Acta*, 2018, **271**, 425–432.
23 H. Kim, S. Suh, S. S. Rao, D. Punnoose, C. V. Tulasivarma, C. V. V. M. Gopi, N. kundakarla, S. Ravi and I. K. Durga, *J. Electroanal. Chem.*, 2016, **777**, 123–132.
24 Y. Li, J. Xu, T. Feng, Q. Yao, J. Xie and H. Xia, *Adv. Funct. Mater.*, 2017, **27**, 1606728.
25 S. Li, C. Yu, J. Yang, C. Zhao, M. Zhang, H. Huang, Z. Liu, W. Guo and J. Qiu, *Energy Environ. Sci.*, 2017, **10**, 1958–1965.
26 J. Zhang, H. Feng, J. Yang, Q. Qin, H. Fan, C. Wei and W. Zheng, *ACS Appl. Mater. Interfaces*, 2015, **39**, 21735–21744.

27 Q. Zhang, B. Zhao, J. Wang, C. Qu, H. Sun, K. Zhang and M. Liu, *Nano Energy*, 2016, **28**, 475–485.

28 M. M. Yadiyar, S. C. Bhise, S. S. Kolekar, J. Chang, K. S. Ghule and A. V. Ghule, *J. Mater. Chem. A*, 2016, **4**, 3504–3512.

29 K. V. Sankar, R. K. Selvan and D. Meyrick, *RSC Adv.*, 2015, **5**, 99959–99967.

30 J. Zhu, Z. Xu and B. Lu, *Nano Energy*, 2014, **7**, 114–123.

31 J. Zhang, H. Feng, J. Yang, Q. Qin, H. Fan, C. Wei and W. Zheng, *ACS Appl. Mater. Interfaces*, 2015, **39**, 21735–21744.

32 Y. Cui, J. Zhang, G. Li, Y. Sun, G. Zhang and W. Zheng, *Chem. Eng. J.*, 2017, **325**, 424–432.

33 N. Tronganh, Y. Gao, W. Jiang, H. Tao, S. Wang, B. Zhao, Y. Jiang, Z. Chen and Z. Jiao, *Appl. Surf. Sci.*, 2018, **439**, 386–393.

34 X. Li, J. Shen, N. Li and M. Ye, *J. Power Sources*, 2015, **282**, 194–201.

35 K. Huang, J. Zhong, Y. Liu and Y. Liu, *Int. J. Hydrogen Energy*, 2015, **40**, 10158–10167.

36 D. Yuan, G. Huang, F. Zhang, D. Yin and L. Wang, *Electrochim. Acta*, 2016, **203**, 238–245.

37 D. Guo, X. Song, L. Tan, H. Ma, H. Pang, X. Wang and L. Zhang, *ACS Sustain. Chem. Eng.*, 2019, **2**, 2803–2810.

38 Z. Li, L. Zhang, B. Li, Z. Liu, Z. Liu, Z. Liu, H. Wang and Q. Li, *Chem. Eng. J.*, 2017, **313**, 1242–1250.

39 S. Ye, J. Feng and P. Wu, *ACS Appl. Mater. Interfaces*, 2013, **15**, 7122–7129.

40 Z. Xing, Q. Chu, X. Ren, C. Ge, A. H. Qusti, A. M. Asiri, A. O. Al-Youbi and X. Sun, *J. Power Sources*, 2014, **245**, 463–467.

41 Y. Tang, T. Chen, S. Yu, Y. Qiao, S. Mu, J. Hu and F. Gao, *J. Mater. Chem. A*, 2015, **3**, 12913–12919.

42 Y. Lu, X. Liu, W. Wang, J. Cheng, H. Yan, C. Tang, J. Kim and Y. Luo, *Sci. Rep.*, 2015, **5**, 16584–16595.

43 S. H. Aboutalebi, A. T. Chidembo, M. Salari, K. Konstantinov, D. Wexler, H. Liu and S. Dou, *Energy Environ. Sci.*, 2011, **4**, 1855–1865.

44 L. Su, L. Gao, Q. Du, L. Hou, X. Yin, M. Feng, W. Yang, Z. Ma and G. Shao, *ACS Sustain. Chem. Eng.*, 2017, **5**, 9945–9954.

45 M. Yan, Y. Yao, J. Wen, L. Long, M. Kong, G. Zhang, X. Liao, G. Yin and Z. Huang, *ACS Appl. Mater. Interfaces*, 2016, **8**, 24525–24535.

46 J. Tang, J. Shen, N. Li and M. Ye, *Ceram. Int.*, 2015, **41**, 6203–6211.

47 W. Chen, P. Yuan, S. Guo, S. Gao, J. Wang, M. Li, F. Liu, J. Wang and J. P. Cheng, *J. Electroanal. Chem.*, 2019, **836**, 134–142.

48 Q. Pan, X. Yang, X. Yang, L. Duan and L. Zhao, *RSC Adv.*, 2018, **8**, 17754–17763.